LETTERS
PUBLISHED ONLINE: 4 JULY 2017 | DOI: 10.1038/NPHYS4182

nature physics

Higgs amplitude mode in a two-dimensional quantum antiferromagnet near the quantum critical point

Tao Hong[1]*, Masashige Matsumoto[2], Yiming Qiu[3], Wangchun Chen[3,4], Thomas R. Gentile[3], Shannon Watson[3], Firas F. Awwadi[5], Mark M. Turnbull[6], Sachith E. Dissanayake[1], Harish Agrawal[7], Rasmus Toft-Petersen[8], Bastian Klemke[8], Kris Coester[9], Kai P. Schmidt[10] and David A. Tennant[1]

Spontaneous symmetry-breaking quantum phase transitions play an essential role in condensed-matter physics[1–3]. The collective excitations in the broken-symmetry phase near the quantum critical point can be characterized by fluctuations of phase and amplitude of the order parameter. The phase oscillations correspond to the massless Nambu–Goldstone modes whereas the massive amplitude mode, analogous to the Higgs boson in particle physics[4,5], is prone to decay into a pair of low-energy Nambu–Goldstone modes in low dimensions[2,6,7]. Especially, observation of a Higgs amplitude mode in two dimensions is an outstanding experimental challenge. Here, using inelastic neutron scattering and applying the bond-operator theory, we directly and unambiguously identify the Higgs amplitude mode in a two-dimensional $S = 1/2$ quantum antiferromagnet $C_9H_{18}N_2CuBr_4$ near a quantum critical point in two dimensions. Owing to an anisotropic energy gap, it kinematically prevents such decay and the Higgs amplitude mode acquires an infinite lifetime.

The Higgs boson appears as the amplitude fluctuation of the condensed Higgs field in the Standard Model of particle physics. Since its discovery, there has been much interest in searching for similar Higgs boson-like particles in condensed-matter physics, such as in superconductors[8–10], charge-density-wave systems[11,12], ultracold bosonic systems[13], and antiferromagnets[14–16]. Strictly speaking, only superconductors are analogous to the particle physics from the point that the gauge field (photon) coupling to the condensate acquires its mass (Meissner effect) by means of symmetry breaking (Anderson–Higgs mechanism). In a broad sense, nevertheless, the excitation mode of the amplitude fluctuation of the order parameter is also termed as 'Higgs amplitude mode' in condensed-matter physics[17]. These works provided new insights about the fundamental theories underlying these exotic materials.

The Higgs amplitude mode is expected in the proximity of a quantum critical point (QCP) but can decay into a pair of low-energy Nambu–Goldstone modes which makes it experimentally difficult to detect. In three-dimensional (3D) systems, where the QCP is a Gaussian fixed point, the Higgs amplitude mode is well defined near the QCP[18]. In contrast, in the two-dimensional (2D) case, where the longitudinal susceptibility becomes infrared divergent near the QCP, it has been debated whether the Higgs amplitude mode may not survive or it is still visible in terms of a scalar susceptibility[6,7,19–23]. Indeed, the Higgs amplitude mode in 2D was evidenced by the scalar response for an ultracold atomic gas near the superfluid to Mott-insulator transition[13], although the observed spectral function is heavily damped. Note that when the Nambu–Goldstone modes become gapped, there is no such physical infrared singularity. In the following paper, we will demonstrate observation of a sharp Higgs amplitude mode through the longitudinal response being such a case in an $S = 1/2$ 2D coupled-ladder compound $C_9H_{18}N_2CuBr_4$ (abbreviated as DLCB) in the vicinity of a QCP in two dimensions.

The quantum $S = 1/2$ Heisenberg antiferromagnetic two-leg spin ladder is one of the cornerstone models in low-dimensional quantum magnetism[24,25]. In the one-dimensional limit of isolated spin-1/2 ladders, the ground state consists of dressed valence-bond singlets on each rung of the ladder. Interestingly, the ground state as shown in Fig. 1a can be tuned by the inter-ladder coupling from the quantum disordered (QD) state, through the QCP, to the renormalized classical regime of a long-range magnetically ordered (LRO) state[26,27]. In the QD phase, the magnetic excitations are triply degenerate magnons with a spin gap energy Δ which vanishes on approach to the QCP. In the LRO phase, the triplet modes evolve into two gapless Nambu–Goldstone modes reflecting spin fluctuations perpendicular to the ordered moment, accompanied by a longitudinal mode (LM) reflecting spin fluctuations along the ordered moment. The latter mode has a gap which grows continuously with the moment and is analogous to the Higgs amplitude mode. Such a LM is usually unstable and decays into a pair of transverse modes, as observed in the $S = 1/2$ coupled Heisenberg chain compound $KCuF_3$, and has a finite lifetime[28,29].

In our previous work[30,31], we have shown that the metal–organic compound DLCB is a unique spin ladder material where the inter-ladder coupling is sufficiently strong to drive the system into the magnetically ordered phase. Figure 1b shows the molecular two-leg ladder structure of DLCB. The collinear magnetic structure was determined by the unpolarized neutron diffraction technique and

[1]Quantum Condensed Matter Division, Oak Ridge National Laboratory, Oak Ridge, Tennessee 37831, USA. [2]Department of Physics, Shizuoka University, Shizuoka 422-8529, Japan. [3]National Institute of Standards and Technology, Gaithersburg, Maryland 20899, USA. [4]Department of Materials Science and Engineering, University of Maryland, College Park, Maryland 20742, USA. [5]Department of Chemistry, The University of Jordan, Amman 11942, Jordan. [6]Carlson School of Chemistry and Biochemistry, Clark University, Worcester, Massachusetts 01610, USA. [7]Instrument and Source Division, Oak Ridge National Laboratory, Oak Ridge, Tennessee 37831, USA. [8]Helmholtz-Zentrum Berlin für Materialien und Energie, D-14109 Berlin, Germany. [9]Lehrstuhl für Theoretische Physik I, TU Dortmund, D-44221 Dortmund, Germany. [10]Lehrstuhl für Theoretische Physik I, Staudtstrasse 7, Universität Erlangen-Nürnberg, D-91058, Germany. *e-mail: hongt@ornl.gov

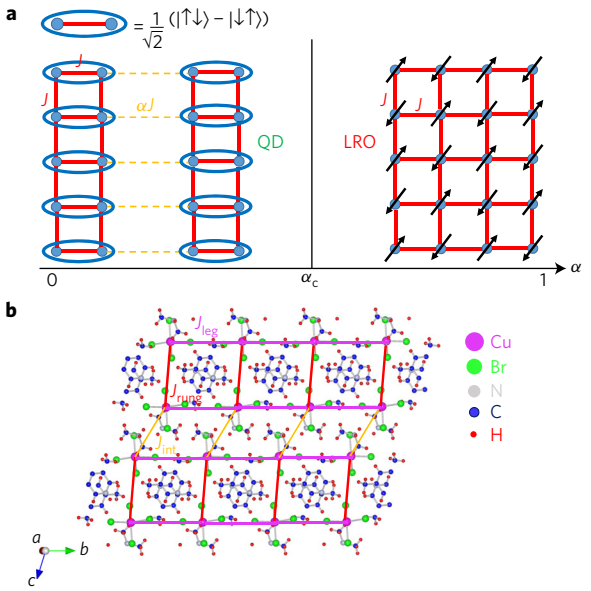

Figure 1 | The two-dimensional spin-1/2 coupled two-leg spin ladder antiferromagnet. a, Schematic diagram of coupled two-leg square spin ladders, where the ground state can be tuned by the inter-ladder coupling αJ from the quantum disordered (QD) phase, through a quantum critical point α_c in two dimensions, to the long-range magnetically ordered (LRO) phase. Blue circles stand for the spin-1/2 magnetic ions. The ellipses represent a singlet valence bond of spins. **b**, The molecular two-leg ladder structure with the leg direction along the crystalline *b* axis and a two-dimensional model for the magnetic interactions in $C_9H_{18}N_2CuBr_4$. Pink, red, and yellow bonds indicate the nearest-neighbour leg, rung, and inter-ladder exchange constants, respectively.

the staggered moments point along the c* axis ($\equiv \hat{\mathbf{z}}$) with a reduced moment size of approximately $0.4\mu_B$ (ref. 30). A minimal 2D spin-interacting model was proposed based on the crystal structure, and the corresponding spin Hamiltonian can be written as:

$$\begin{aligned} H = {} & J_{\rm rung}\sum_{l,i}(\lambda \mathbf{S}^x_{l_1,i}\mathbf{S}^x_{l_2,i} + \lambda \mathbf{S}^y_{l_1,i}\mathbf{S}^y_{l_2,i} + \mathbf{S}^z_{l_1,i}\mathbf{S}^z_{l_2,i}) \\ & + J_{\rm leg}\sum_{l,i}(\lambda \mathbf{S}^x_{l_1,i}\mathbf{S}^x_{l_1,i+1} + \lambda \mathbf{S}^y_{l_1,i}\mathbf{S}^y_{l_1,i+1} + \mathbf{S}^z_{l_1,i}\mathbf{S}^z_{l_1,i+1} \\ & + \lambda \mathbf{S}^x_{l_2,i}\mathbf{S}^x_{l_2,i+1} + \lambda \mathbf{S}^y_{l_2,i}\mathbf{S}^y_{l_2,i+1} + \mathbf{S}^z_{l_2,i}\mathbf{S}^z_{l_2,i+1}) \\ & + J_{\rm int}\sum_{l,i}(\lambda \mathbf{S}^x_{l_1,i}\mathbf{S}^x_{(l-1)_2,i} + \lambda \mathbf{S}^y_{l_1,i}\mathbf{S}^y_{(l-1)_2,i} + \mathbf{S}^z_{l_1,i}\mathbf{S}^z_{(l-1)_2,i} \\ & + \lambda \mathbf{S}^x_{l_2,i}\mathbf{S}^x_{(l+1)_1,i} + \lambda \mathbf{S}^y_{l_2,i}\mathbf{S}^y_{(l+1)_1,i} + \mathbf{S}^z_{l_2,i}\mathbf{S}^z_{(l+1)_1,i}) \end{aligned} \quad (1)$$

where *l* indexes the site of a ladder, *i* indexes rungs, and 1 and 2 stand for each leg. $J_{\rm rung}$, $J_{\rm leg}$, and $J_{\rm int}$ are the nearest-neighbour rung, leg, and inter-ladder exchange constants. λ (between 0 and 1) specifies an exchange anisotropy, with $\lambda = 0$ or 1 being the limiting case of Ising or Heisenberg interactions. Indeed, the observed magnon dispersions can be described by this model quantitatively[30]. The observed spin gap energy $\Delta = 0.32(3)$ meV is due to a small Ising anisotropy. Further evidence for the two-dimensionality is provided by a measurement of the inter-layer dispersion (Supplementary Fig. 1b).

Importantly, the analysis of the spin Hamiltonian indicates that DLCB is close to a QCP[30], making DLCB an ideal $S = 1/2$ quantum antiferromagnet to investigate the Higgs amplitude mode. The more detailed examination of this QCP was analysed by tuning the inter-rung interactions (Supplementary Fig. 2). In the easy-axis case, the U(1) symmetry is not spontaneously broken in the ordered phase, and the two branches of transverse modes (TMs) would have equal gap energies as predicted by the spin-wave theory. Therefore, if the LM/Higgs amplitude mode is sufficiently close to TMs, it could become kinematically unable to decay in this region, and thus acquire an infinite lifetime.

Since TMs and the LM could be degenerate within the instrumental resolution in DLCB, we carried out a follow-up unpolarized inelastic neutron-scattering (INS) study in an external magnetic field. In terms of the *z* component of total spin *S*, two species of TMs have $S_z = \pm 1$ whereas the LM has $S_z = 0$. To make S_z a good quantum number, the field direction has to be aligned along the easy-axis and a horizontal-field cryomagnet was employed for that purpose. With an applied field $\mu_0 H$, the Zeeman energy term is $g\mu_B\mu_0 H S_z$, where *g* is the Landé *g*-factor and μ_B is the Bohr magneton. Thus, the energy shifts of TMs are expected to be $\pm g\mu_B\mu_0 H$ while the LM should remain unchanged. Consequently, if the splitting is large enough, the LM could be identified by this Zeeman effect.

Figure 2a shows the zero-field background-subtracted energy scan at the magnetic zone centre $\mathbf{q} = (0.5, -0.5, 1.5)$ and $T = 50$ mK. The spectral lineshape was modelled by superposition of two double-Lorentzian damped harmonic-oscillator (DHO) models convolved with the instrumental resolution function[32,33]. The best fit yields the gap energies of TMs ($S_z = \pm 1$) and the LM ($S_z = 0$) as $\Delta_{\rm TM} = 0.34(3)$ meV and $\Delta_{\rm LM} = 0.48(3)$ meV, respectively. At $\mu_0 H = 1$ T in Fig. 2b, TMs ($S_z = \pm 1$) are split into two branches. The observed quasielastic neutron scattering hinders observation of TM ($S_z = 1$) at $\mu_0 H = 1.5$ T in Fig. 2c. At $\mu_0 H = 2$ T in Fig. 2d, TM ($S_z = 1$) is merged into the elastic line while the LM becomes clearly visible and well distinguished from TM ($S_z = -1$). Figure 2e summarizes the measured field dependences of $\Delta_{\rm TMs}(S_z = \pm 1)$ and $\Delta_{\rm LM}$ ($S_z = 0$). $\Delta_{\rm TMs}$ ($S_z = \pm 1$) as a function of field agree well with the Zeeman spectral splitting $\pm g\mu_B\mu_0 H$ using $g = 2.15$ and the LM is indeed field-independent within the experimental uncertainties. The small discrepancy between data and calculations at 2 T is due to the occurrence of a spin-flop transition (Supplementary Fig. 3). The analysis also indicates that the peak profile of the Higgs amplitude mode in each field is limited by the instrumental resolution within experimental uncertainty, as shown in Fig. 2f. In other words, decay of the LM/Higgs amplitude mode ($S_z = 0$) into a TM ($S_z = 1$) and another TM ($S_z = -1$) is forbidden by the kinematic conditions. However, because of the limited access of the reciprocal space using a horizontal-field cryomagnet, we could not map out the excitation spectra in the Brillouin zone (BZ).

Another straightforward way to unambiguously determine the nature of spin polarization of magnetic excitation spectra is by the polarized neutron-scattering method. In general, however, it is fairly challenging to carry out the polarized INS because of significant loss of neutron intensity due to neutron polarization arrangements compared with unpolarized neutron arrangements. To compensate for that, the polarized neutron data were collected using a high-flux cold neutron spectrometer. The polarization analysis was performed using the recently developed capability of wide-angle ^{3}He spin filters[34]. Figure 3a shows the θ-scans of the nuclear Bragg reflection $(0, 1, -1)$ at $T = 1.4$ K with the non-spin-flip (NSF) and spin-flip (SF) configurations, respectively. The flipping ratio *F* can be calculated as $I_{\rm NSF}/I_{\rm SF} \simeq 43(1)$, which corresponds to an overall polarization efficiency of $(F-1)/(F+1) = 0.95$. Furthermore, Fig. 3b shows the background-subtracted θ-scans of the magnetic Bragg reflection $(0.5, 0.5, -0.5)$ at $T = 1.4$ K with the NSF and SF configurations, respectively. The scattering intensity in the NSF channel dominates over that in the SF channel, suggesting that the out-of-plane spin component is dominant, and thus confirming the determined orientation of the staggered moments.

With the high efficiency of neutron spin filters firmly established and the magnetic spin structure in DLCB well determined, we proceed to investigate the spin dynamics using polarized neutrons.

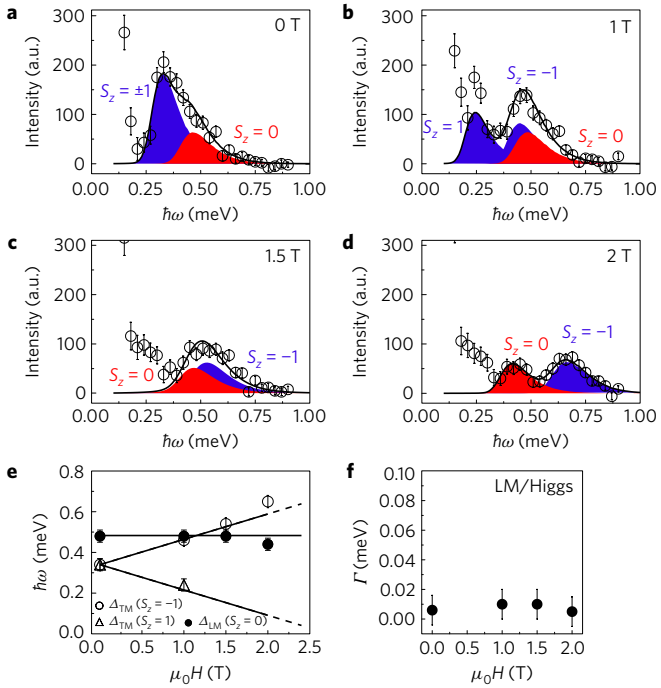

Figure 2 | The Zeeman effect. a–d, The background-subtracted energy scans at the magnetic zone centre $\mathbf{q} = (0.5, -0.5, 1.5)$, $T = 50$ mK and $\mu_0 H = 0$ (**a**), $\mu_0 H = 1$ T (**b**), $\mu_0 H = 1.5$ T (**c**) and $\mu_0 H = 2$ T (**d**). Solid lines are fits to a double-Lorentzian damped harmonic-oscillator model convolved with the instrumental resolution function and filled areas represent the contribution from the transverse modes (TMs, blue) and the longitudinal mode (LM, red) or the Higgs amplitude mode. **e**, Field dependences of TMs ($S_z = \pm 1$) and the LM ($S_z = 0$). The dashed lines are the calculated Zeeman energy term as described in the text. The solid lines are the calculations by the bond-operator theory as described in the text. **f**, Field dependence of resolution-corrected intrinsic linewidth of the Higgs amplitude mode. Error bars represent one standard deviation.

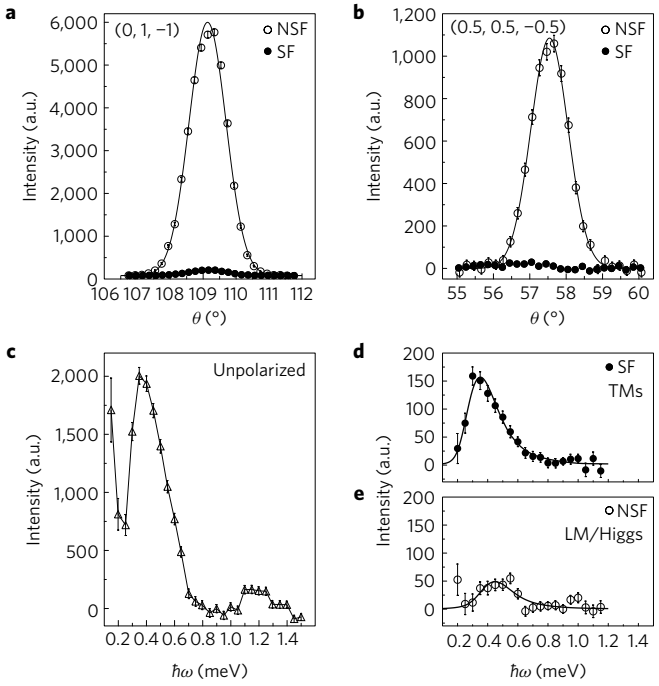

Figure 3 | Feasibility of the polarized neutron study. a,**b**, Background-subtracted θ-scans at the nuclear Bragg reflection (0, 1, −1) (**a**) and the magnetic Bragg reflection (0.5, 0.5, −0.5) (**b**) with non-spin-flip (NSF) and spin-flip (SF) configurations, respectively. Solid lines are fits to a Gaussian function. **c**–**e**, The background-subtracted transferred energy scans at the magnetic zone centre $\mathbf{q} = (0.5, 0.5, -0.5)$ with unpolarized neutron (**c**), SF (**d**) and NSF (**e**) configurations, respectively. Solid lines are fits to a two-Lorentzian damped harmonic-oscillator model convolved with the instrumental resolution function. All experimental data were collected at $T = 1.4$ K. Error bars represent one standard deviation.

The experiment was designed in such a way that TMs and the LM can be separated from each other in the SF and NSF configurations, respectively (for further details, see Methods). For the comparison purposes, Fig. 3c shows the background-subtracted energy scan at $\mathbf{q} = (0.5, 0.5, -0.5)$ and $T = 1.4$ K using unpolarized neutrons. Figure 3d,e shows the same energy scans with the SF and NSF configurations, respectively. And data were fitted to the same DHO model convolved with the instrumental resolution function. The spin gap energies of TMs and the LM/Higgs amplitude mode were obtained as $\Delta_{TMs} = 0.33(3)$ meV and $\Delta_{LM} = 0.48(3)$ meV, in excellent agreement with the results from the Zeeman effect. The spectral weight ratio between them is approximately 2.6:1.

After confirming the feasibility of such a challenging experiment, we managed to map out the excitation spectra in the BZ. Serving as a reference, Fig. 4a,b shows the false-colour maps of the spin-wave spectra along two high-symmetry directions in the reciprocal-lattice space using unpolarized neutrons. With the SF configuration, as expected, the magnetic excitation spectra in Fig. 4c,d are in excellent agreement with the calculations using SPINW[35] in the linear spin-wave theory (LSWT) approximation, and thus was confirmed as TMs. The Hamiltonian parameters of $J_{leg} = 0.64$ meV, $J_{rung} = 0.70$ meV, $J_{int} = 0.19$ meV, and $\lambda = 0.95$ provide the best agreement with experimental data. The modelled dispersion curves in Fig. 4c,d are close to the quantitative calculations using the high-order series expansions[30].

Since the one-magnon excitation of the LM is not predicted in LSWT, to analyse the experimental data with the NSF configuration, we employed the bond-operator theory (BOT) for the description of the low-energy excitations in the vicinity of the QCP on DLCB. The detailed description of the harmonic BOT can be found in refs 36–39. The ordered moment is estimated as 38.5% of the saturation value and is consistent with the experimental value of 37(5)%. The exchange interaction parameters were extracted as $J_{leg} = 0.57$ meV, $J_{rung} = 1.21$ meV, $J_{int} = 0.11$ meV, and $\lambda = 0.95$ from the best fit. Note that the extracted parameters correspond to the renormalized parameters within the scope of harmonic BOT. Since DLCB is a weakly interacting ladder system, J_{rung} and J_{leg} are strongly renormalized (the former and latter are enhanced and reduced, respectively)[40,41]. Therefore, J_{rung} is markedly larger than J_{leg}. The solid green lines in Fig. 4e,f shows the calculated LM (Higgs amplitude mode) with a gap energy at 0.48 meV. We notice that the BOT calculation in Fig. 4f increases monotonically and deviates from the experimental data at the zone boundary, which may originate from the fact that the BOT is a mean-field treatment and application of this technique to the low-dimensional system could be limited. For the low-energy excitations, nevertheless, it works well in both QD and LRO phases. For instance, as shown in Fig. 2e, the agreement of the field dependence of the Zeeman energy term between the experimental data and the calculations by BOT is excellent.

Figure 4e,f shows the calculated excitation spectra by BOT, which reproduce the experimental data qualitatively. Thus, our conclusion that the nature of spin excitation observed in the NSF configuration is due to spin fluctuation along the staggered moment direction is fairly convincing. Note that the Higgs amplitude mode in DLCB is distinctly different from the longitudinal excitations in the $S = 1/2$ 2D Heisenberg square-lattice (HSL) antiferromagnet $Cu(DCOO)_2 \cdot 4D_2O$ (CFTD)[42,43] because the $S = 1/2$ 2D HSL

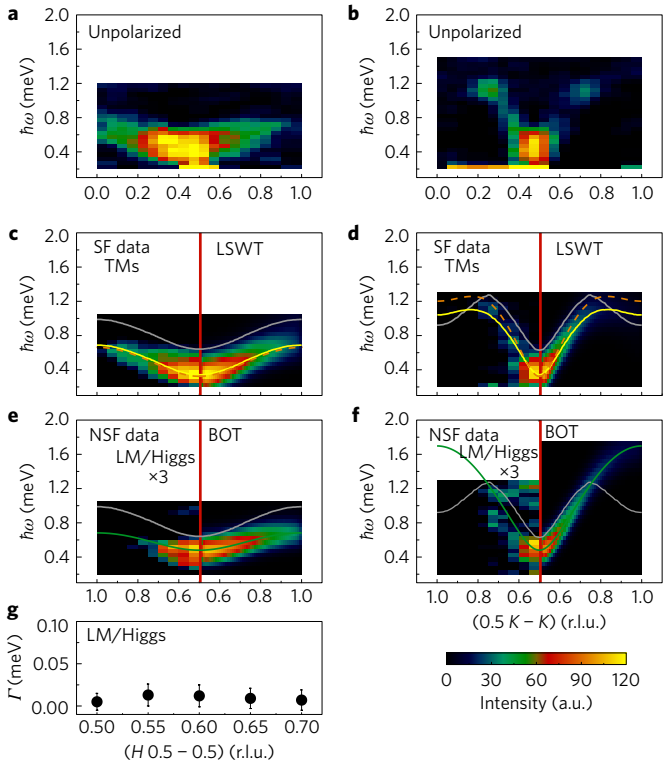

Figure 4 | Polarized neutron study of the spin dynamics. a,**b**, False-colour maps of the background-subtracted magnetic excitation spectra as a function of energy and wavevector transfer measured by unpolarized neutrons. **c**,**d**, Comparison of data with the spin-flip (SF) configuration and the calculation by the linear spin-wave theory (LSWT). **e**,**f**, Comparison of data with the non-spin-flip (NSF) configuration and the calculation by the bond-operator theory (BOT) along the $(H0.5-0.5)$ and $(0.5K-K)$ directions, respectively. Intensity was enlarged by a factor of three. Dashed brown lines are the calculation using the high-order series expansions. Solid yellow lines are the transverse modes calculated by LSWT. Solid green lines are the longitudinal (Higgs amplitude) modes calculated by BOT. Solid grey lines are the calculated lower boundary of the two-magnon continuum. **g**, Wavevector dependence of the resolution-corrected intrinsic linewidth Γ of the Higgs amplitude mode. Note that Γ along $(0.5K-K)$ cannot be reliably extracted due to the weak intensity. All experimental data were collected at $T=1.4$ K.

antiferromagnet is far from the QCP and the observed longitudinal spectra in CFTD originate from the two-magnon continuum. Consequently, the spectral lineshapes are broadened. Recent theoretical work[44,45] suggests that there is a prominent resonance, which was proposed as a Higgs resonance with finite lifetime, inside the continuum due to the attractive magnon–magnon interaction. Moreover, the grey lines in Fig. 4e,f are the calculated lower boundary of the two-magnon continuum in DLCB, which lies well above the Higgs amplitude mode. Hence, the spontaneous decay of the Higgs amplitude mode into a pair of TMs is forbidden due to violation of the laws of energy and momentum conservation, as evidenced by the wavevector dependence of the intrinsic linewidth Γ, which is limited by the instrumental resolution, as shown in Fig. 4g. It is worth pointing out that the Higgs amplitude mode is also evident from the excitation spectra with an external magnetic field applied perpendicularly to the easy-axis[31]. In that case, the Higgs amplitude mode is stable at low fields and the decay occurs beyond the crossover with the lower boundary of the two-magnon continuum at $\sim$1.5 T.

In summary, the unique ability of neutron scattering to probe the spin polarization of dynamic spin pair-correlation functions allows one to distinguish the Higgs amplitude mode from the dominant transverse Nambu–Goldstone modes in the two-dimensional $S=1/2$ antiferromagnet DLCB. The transverse modes have a finite excitation gap energy due to a weak Ising anisotropy. The opening of the gap kinematically prevents the decay process from the Higgs amplitude mode to a pair of transverse modes. This leads to the long lifetime for the Higgs amplitude mode and makes it observable near the quantum critical point in two dimensions.

Note added in proof: Recently we became aware of an INS work[46] that reports the Higgs amplitude mode in a 2D antiferromagnet Ca_2RuO_4.

Methods

Methods, including statements of data availability and any associated accession codes and references, are available in the online version of this paper.

Received 26 September 2016; accepted 23 May 2017; published online 4 July 2017

References

1. Sondhi, S. L., Girvin, S. M., Carini, J. P. & Shahar, D. Continuous quantum phase transitions. *Rev. Mod. Phys.* **69,** 315–333 (1997).
2. Sachdev, S. *Quantum Phase Transitions* (Cambridge Univ. Press, 1999).
3. Vojta, M. Quantum phase transitions. *Rep. Prog. Phys.* **66,** 2069–2110 (2003).
4. Higgs, P. W. Broken symmetries and the masses of gauge bosons. *Phys. Rev. Lett.* **13,** 508–509 (1964).
5. Guralnik, G. S., Hagen, C. R. & Kibble, T. W. B. Global conservation laws and massless particles. *Phys. Rev. Lett.* **13,** 585–587 (1964).
6. Chubukov, A. V., Sachdev, S. & Ye, J. Theory of two-dimensional quantum Heisenberg antiferromagnets with a nearly critical ground state. *Phys. Rev. B* **49,** 11919–11961 (1994).
7. Sachdev, S. Universal relaxational dynamics near two-dimensional quantum critical points. *Phys. Rev. B* **59,** 14054–14073 (1999).
8. Sooryakumar, R. & Klein, M. V. Raman Scattering by superconducting-gap excitations and their coupling to charge-density waves. *Phys. Rev. Lett.* **45,** 660–662 (1980).
9. Littlewood, P. B. & Varma, C. M. Amplitude collective modes in superconductors and their coupling to charge-density waves. *Phys. Rev. B* **26,** 4883–4893 (1982).
10. Matsunaga, R. *et al*. Light-induced collective pseudospin precession resonating with Higgs mode in a superconductor. *Science* **345,** 1145–1149 (2014).
11. Tsang, J. C., Smith, J. E. & Shafer, M. W. Raman spectroscopy of soft modes at the charge-density-wave phase transition in 2H-NbSe. *Phys. Rev. Lett.* **37,** 1407–1410 (1976).
12. Pouget, J. P., Hennion, B., Escribe-Filippini, C. & Sato, M. Neutron-scattering investigations of the Kohn anomaly and of the phase and amplitude charge-density-wave excitations of the blue bronze $K_{0.3}MoO_3$. *Phys. Rev. B* **43,** 8421–8430 (1991).
13. Endres, M. *et al*. The 'Higgs' amplitude mode at the two-dimensional superfluid/Mott insulator transition. *Nature* **487,** 454–458 (2012).
14. Rüegg, Ch. *et al*. Quantum magnets under pressure: controlling elementary excitations in $TlCuCl_3$. *Phys. Rev. Lett.* **100,** 205701 (2008).
15. Merchant, P. *et al*. Quantum and classical criticality in a dimerized quantum antiferromagnet. *Nat. Phys.* **10,** 373–379 (2014).
16. Grenier, B. *et al*. Longitudinal and transverse Zeeman ladders in the Ising-like chain antiferromagnet $BaCo_2V_2O_8$. *Phys. Rev. Lett.* **114,** 017201 (2015).
17. Pekker, D. & Varma, C. M. Amplitude/Higgs modes in condensed matter physics. *Annu. Rev. Condens. Matter Phys.* **6,** 269–297 (2015).
18. Lohöfer, M. & Wessel, S. Excitation-gap scaling near quantum critical three-dimensional antiferromagnets. *Phys. Rev. Lett.* **118,** 147206 (2017).
19. Podolsky, D., Auerbach, A. & Arovas, D. P. Visibility of the amplitude (Higgs) mode in condensed matter. *Phys. Rev. B* **84,** 174522 (2011).
20. Pollet, L. & Prokof'ev, N. Higgs mode in a two-dimensional superfluid. *Phys. Rev. Lett.* **109,** 010401 (2012).
21. Gazit, S., Podolsky, D. & Auerbach, A. Fate of the Higgs mode near quantum criticality. *Phys. Rev. Lett.* **110,** 140401 (2013).
22. Chen, K., Liu, L., Deng, Y., Pollet, L. & Prokof'ev, N. Universal properties of the Higgs resonance in (2+1)-dimensional U(1) critical systems. *Phys. Rev. Lett.* **110,** 170403 (2013).
23. Lohöfer, M. *et al*. Dynamical structure factors and excitation modes of the bilayer Heisenberg model. *Phys. Rev. B* **92,** 245137 (2015).

24. Barnes, T., Dagotto, E., Riera, J. & Swanson, E. S. Excitation spectrum of Heisenberg spin ladders. *Phys. Rev. B* **47,** 3196–3203 (1993).
25. Dagotto, E. & Rice, T. M. Surprise on the way from one- to two-dimensional quantum magnets: the ladder materials. *Science* **271,** 618–623 (1996).
26. Troyer, M., Zhitomirsky, M. E. & Ueda, K. Near critical ground state of $LaCuO_{2.5}$. *Phys. Rev. B* **55,** R6117(R) (1997).
27. Normand, B. & Rice, T. M. Dynamical properties of an antiferromagnet near the quantum critical point: application to $LaCuO_{2.5}$. *Phys. Rev. B* **56,** 8760–8773 (1997).
28. Lake, B., Tennant, D. A. & Nagler, S. E. Novel longitudinal mode in the coupled quantum chain compound $KCuF_3$. *Phys. Rev. Lett.* **85,** 832–835 (2000).
29. Lake, B., Tennant, D. A. & Nagler, S. E. Longitudinal magnetic dynamics and dimensional crossover in the quasi-one-dimensional spin-1/2 Heisenberg antiferromagnetic $KCuF_3$. *Phys. Rev. B* **71,** 134412 (2005).
30. Hong, T. *et al*. Magnetic ordering induced by interladder coupling in the spin-1/2 Heisenberg two-leg ladder antiferromagnet $C_9H_{18}N_2CuBr_4$. *Phys. Rev. B* **89,** 174432 (2014).
31. Hong, T. *et al*. Field induced spontaneous quasiparticle decay and renormalization of quasiparticle dispersion in a quantum antiferromagnet. *Nat. Commun.* **8,** 15148 (2017).
32. Hong, T. *et al*. Effect of pressure on the quantum spin ladder material IPA-$CuCl_3$. *Phys. Rev. B* **78,** 224409 (2008).
33. Hong, T. *et al*. Neutron scattering study of a quasi-two-dimensional spin-1/2 dimer system: piperazinium hexachlorodicuprate under hydrostatic pressure. *Phys. Rev. B* **82,** 184424 (2010).
34. Chen, W. C. *et al*. Recent advancements of wide-angle polarization analysis with ^{3}He neutron spin filters. *J. Phys. Conf. Ser.* **746,** 012016 (2016).
35. Toth, S. & Lake, B. Linear spin wave theory for single-Q incommensurate magnetic structures. *J. Phys. Condens. Matter* **27,** 166002 (2015).
36. Sommer, T., Vojta, M. & Becker, K. W. Magnetic properties and spin waves of bilayer magnets in a uniform field. *Eur. Phys. J. B* **23,** 329–339 (2001).
37. Matsumoto, M., Normand, B., Rice, T. M. & Sigrist, M. Magnon dispersion in the field-induced magnetically ordered phase of $TlCuCl_3$. *Phys. Rev. Lett.* **89,** 077203 (2002).
38. Matsumoto, M., Normand, B., Rice, T. M. & Sigrist, M. Field- and pressure-induced magnetic quantum phase transitions in $TlCuCl_3$. *Phys. Rev. B* **69,** 054423 (2004).
39. Shiina, R., Shiba, H., Thalmeier, P., Takanashi, A. & Sakai, O. Dynamics of multipoles and neutron scattering spectra in quadrupolar ordering phase of CeB_6. *J. Phys. Soc. Jpn* **72,** 1216–1225 (2003).
40. Gopalan, S., Rice, T. M. & Sigrist, M. Spin ladders with spin gaps: a description of a class of cuprates. *Phys. Rev. B* **49,** 8901–8910 (1994).
41. Normand, B. & Rüegg, Ch. Complete bond-operator theory of the two-chain spin ladder. *Phys. Rev. B* **83,** 054415 (2011).
42. Christensen, N. B. *et al*. Quantum dynamics and entanglement of spins on a square lattice. *Proc. Natl Acad. Sci. USA* **104,** 15264–15269 (2007).
43. Dalla Piazza, B. *et al*. Fractional excitations in the square-lattice quantum antiferromagnet. *Nat. Phys.* **11,** 62–68 (2015).
44. Powalski, M., Uhrig, G. S. & Schmidt, K. P. Roton minimum as a fingerprint of magnon-Higgs scattering in ordered quantum antiferromagnets. *Phys. Rev. Lett.* **115,** 207202 (2015).
45. Powalski, M., Schmidt, K. P. & Uhrig, G. S. Mutally attacting spin waves in the square-lattice quantum antiferromagnet. Preprint at http://arxiv.org/abs/1701.04730 (2017).
46. Jain, A. *et al*. Higgs mode and its decay in a two-dimensional antiferromagnet. *Nat. Phys.* (2017).

Acknowledgements

T.H. thanks C. D. Batista for the insightful discussion, Q. Ye for the initial neutron polarization set-up and R. Erwin for the development of ^{3}He efficiency correction software. T.H. also thanks D. L. Q. Castro, Z. L. Lu and Z. Hüsges for the assistance during the experiment. One of the authors (M.M.) is supported by JSPS KAKENHI Grant Number 26400332. A portion of this research used resources at the High Flux Isotope Reactor, a DOE Office of Science User Facility operated by the Oak Ridge National Laboratory. Access to MACS was provided by the Center for High Resolution Neutron Scattering, a partnership between NIST and NSF under Agreement No. DMR-1508249.

Author contributions

T.H. conceived the project. F.F.A. and M.M.T. prepared the samples. The polarization apparatus and corrections were provided by W.C., T.R.G. and S.W. T.H., Y.Q., H.A., R.T.-P. and B.K. performed the neutron-scattering measurements. T.H., M.M., D.A.T., S.E.D., K.C. and K.P.S. analysed the data. All authors contributed to writing of the manuscript.

Additional information

Supplementary information is available in the online version of the paper. Reprints and permissions information is available online at www.nature.com/reprints. Publisher's note: Springer Nature remains neutral with regard to jurisdictional claims in published maps and institutional affiliations. Correspondence and requests for materials should be addressed to T.H.

Competing financial interests

The authors declare no competing financial interests.

Methods

Single crystal growth. Deuterated single crystals were grown using a solution method[47]. An aqueous solution containing a 1:1:1 ratio of deuterated (DMA)Br, (35DMP)Br, where DMA^+ is the dimethylammonium cation and $35DMP^+$ is the 3,5-dimethylpyridinium cation, and copper(II) bromide was allowed to evaporate over several days in a closed desiccator. A few drops of DBr were added to the solution to avoid hydrolysis of the Cu(II) ion.

Neutron-scattering measurements. Unpolarized neutron-scattering measurements using a horizontal-field superconducting magnet with a dilution fridge insert were carried out on a cold neutron triple-axis spectrometer (FLEXX)[48] at Helmholtz-Zentrum Berlin. The sample consists of two co-aligned deuterated single crystals with a total mass of 2.5 g and a 1.0° mosaic spread and was oriented in the $(H-HL)$ reciprocal-lattice plane. Unpolarized inelastic neutron-scattering measurements using a standard helium-flow cryostat were carried out on a cold neutron triple-axis spectrometer (CTAX) at the High Flux Isotope Reactor, Oak Ridge National Laboratory. Polarized neutron-scattering measurements using a standard helium-flow cryostat were performed on a high-intensity multi-axis crystal spectrometer (MACS)[49] at the NIST Center for Neutron Research. The peak flux at the sample position is approximately 5×10^8 neutrons cm^{-2} s^{-1}. The sample assembly with three co-aligned deuterated single crystals (a total mass of 3.5 g and a 1.0° mosaic spread) was oriented in the $(HK-K)$ reciprocal-lattice plane. In all experiments, the final neutron energy was fixed at 3.0 meV and the energy resolutions of FLEXX and MACS at the elastic line are 0.10 meV and 0.15 meV, respectively. The background was determined at $T=15$ K under the same instrument configurations, and has been subtracted.

Polarized neutron measurements. In the experimental set-up, both incident and outgoing neutron beams were polarized by nuclear spin polarized ^{3}He gas cells. NMR-based inversion of the ^{3}He polarization in the polarizer cell allows polarization of the incident beam parallel or antiparallel to the vertical axis at will. The overall transmission at the beginning of a polarized neutron set-up (each run lasts about two days) is approximately 11% and reduced to approximately 5% before the ^{3}He gas cells change out. The initial flipping ratio F is about 43(1), indicating that the product of the polarizing efficiencies of the NSF cells $PA=(F-1)/(F+1)$ is 95%. Typically, after the two-day operation, F is reduced to 20(1) and PA becomes 91%. Since F was always above 20, the polarization leakage effect is as small as $1/F$ ($\leq$5%). To account for decay of the ^{3}He polarization and neutron transmission with time, the polarized neutron data were corrected by ^{3}He efficiency correction software as described in Supplementary Information.

The principles for polarized neutron scattering can be summarized as follows: phonons and structural scattering are seen in the NSF channel; components of spin fluctuations parallel to the direction of neutron polarization are seen in the NSF channel; components of spin fluctuations perpendicular to the direction of the neutron polarization are seen in the SF channel[50].

The sample was aligned in such a way that the [0,1,1] direction in the real space is vertical. Thus, the angle α between the vertical polarization and staggered moment direction is 17.6°. In this geometry with the NSF configuration, the large fraction ($\cos^2\alpha\simeq91\%$) is due to spin fluctuations along the direction of the staggered moment (LM/the Higgs amplitude mode), while the remaining 9% corresponds to the spin fluctuations perpendicular to the staggered moment (TMs) and is negligible. In contrast, in the SF configuration, TMs have accounted for 91% of the contribution and the Higgs amplitude mode is negligible. Therefore, by employing polarized INS, we are able to separate the Higgs amplitude mode from the TMs in the magnetic excitation spectra. Polarized neutron measurements cover half of Brillouin zone due to the fact that the polarizing efficiency becomes either significantly reduced or not available for small neutron-scattering angles.

Data analysis. The spectral lineshape in Figs 2a–d and 3d–e was fitted to the following double-Lorentzian damped harmonic-oscillator model

$$S(\hbar\omega)=\frac{A}{1-\exp(-\hbar\omega/k_BT)}\left[\frac{\Gamma}{(\hbar\omega-\Delta)^2+\Gamma^2}-\frac{\Gamma}{(\hbar\omega+\Delta)^2+\Gamma^2}\right]$$

where k_B is the Boltzmann constant, Δ is the peak position and Γ is the resolution-corrected intrinsic excitation linewidth, that is, half-width at half-maximum (HWHM) and convolved with the instrumental resolution function. The experimental resolution was calculated using the Reslib software[51].

For the false-colour maps in Fig. 4a–f, data were obtained by combining a series of constant-$\mathbf{q}$ scans along either the $(H0.5-0.5)$ or $(0.5K-K)$ direction with a step size of 0.05 r.l.u. and simulations were convolved with the instrumental resolution function where the neutron polarization factor and the magnetic form factor for Cu^{2+} were included.

A detailed description about the determination of the lower boundary of two-magnon continuum can be found in ref. 31.

Measurement of the inter-layer dispersion. Additional unpolarized inelastic neutron-scattering measurements were performed at MACS to investigate the possible interaction between the two-dimensional layers in DLCB. For that purpose, a single crystal ($\sim$2 g) with a 1.0° mosaic spread was aligned in the (HKH) reciprocal-lattice plane. Supplementary Fig. 1a shows the measured excitation spectrum along the leg direction and the observed dispersions are fully consistent with the calculations by LSWT as described in the main text. Along the inter-layer direction, the dispersion is absent within the instrumental resolution (Supplementary Fig. 1b), indicating that DLCB is an excellent 2D spin-interacting system.

Analysis of the energy gap by tuning the inter-rung interactions. We assume that J_{rung} is fixed and the inter-rung interactions vary as $J^*_{leg}=RJ_{leg}$ and $J^*_{int}=RJ_{int}$, where values of J_{rung}, J_{leg} and J_{int} are obtained as described in the main text. Supplementary Fig. 2 summarizes the calculations by BOT of the evolution of the spin gap energy as a function of the enhancement factor R. At small R, due to the Ising anisotropy, the triplet spin gap energy splits into a singlet ($S_z=0$) and a doublet ($S_z=\pm1$). When R initially increases, the spin gap energies of both the singlet and the doublet decrease. Spin gap of the singlet closes at the QCP while the doublet remains gapped. When R further increases, the softened singlet mode acquires a spin gap again and becomes the Higgs amplitude mode. The analysis indicates that the QCP is located at $R_c=0.923$, which is close to the case in DLCB ($R=1$) and thus confirms our conclusion in the main text. For $R<R_c$, the quantum disordered phase is stabilized, while the long-range ordered phase is stabilized for $R>R_c$. Calculation by BOT of emergence of the staggered moment size as a function of R is also shown in Supplementary Fig. 2.

The spin-flop transition. In DLCB, an application of a magnetic field along the easy-axis direction would lead to the spin reorientation, that is, spin-flop transition. In the spin-flop phase, S_z is no longer a good quantum number. To find out the critical field where the spin reorientation occurs, we measured the field dependence of several magnetic reflections, as shown in Supplementary Fig. 3, at FLEXX using a horizontal-field cryomagnet. The integrated-peak intensities are almost field-independent at low fields, then start to increase above 1.7 T, and finally become saturated above 2.5 T after the spin is flopped for the (0.5, −0.5, −1.5) and (1.5, −1.5, 2.5) magnetic reflections. From the fact that neutron scattering probes the components of spin fluctuation perpendicular to the transferred wavevector, the orientation of the ordered moment in the spin-flop phase is 90° out of the horizontal plane, with the axis of rotation approximately along $\mathbf{q}=(1.5,-1.5,0.5)$. Overall, the above results confirm that in DLCB, when the field direction is aligned parallel to the easy-axis direction, S_z remains as a good quantum number at least up to 1.7 T.

Data availability. The data that support the plots within this paper and other findings of this study are available from the corresponding author upon request.

References

47. Awwadi, F., Willett, R. D., Twamley, B., Schneider, R. & Landee, C. P. Strong rail spin 1/2 antiferromagnetic ladder systems: (Dimethylammonium)(3, 5-Dimethylpyridinium) CuX_4, X= Cl, Br. *Inorg. Chem.* **47,** 9327–9332 (2008).
48. Le, M. D. *et al*. Gains from the upgrade of the cold neutron triple-axis spectrometer FLEXX at the BER-II reactor. *Nucl. Instr. Meth. Phys. Res. A* **729,** 220–226 (2013).
49. Rodriguez, J. A. *et al*. MACS-a new high intensity cold neutron spectrometer at NIST. *Meas. Sci. Technol.* **19,** 034023 (2008).
50. Moon, R. M., Riste, T. & Koehler, W. C. Polarization analysis of thermal-neutron scattering. *Phys. Rev.* **181,** 920–931 (1969).
51. Zheludev, A. ResLib 3.4c (Oak Ridge National Laboratory, 2007).